# Applying Riemann solvers to open boundaries in free surface and confined flows

Antoine Joly, Damien Violeau, Agnès D Leroy, Martin Ferrand

# Applying Riemann solvers to open boundaries in free surface and confined flows

Antoine Joly, Damien Violeau, Agnès Leroy
EDF R&D and Saint-Venant Laboratory for Hydraulics
Chatou, France
antoine.joly@edf.fr

Martin Ferrand
EDF R&D
Chatou, France

***Abstract*—Due to the Lagrangian nature of SPH, dealing with open boundaries (which are intrinsically Eulerian) is a challenging issue. This issue has recently been addressed in the Unified Semi-Analytical Boundaries framework [1], where it has been shown how to properly deal with mass fluxes at the open boundaries. However imposing both velocities and pressures on the open boundaries will over-constrain the problem, and in most cases only one of these quantities will be known. Therefore, Riemann Solvers can be used to calculate and prescribe compatible fields at the open boundaries. These compatible fields allow therefore complex boundary conditions to be imposed.**

## I. Introduction

Due to the nature of SPH method, simulations can have a high computational cost. As such, it becomes of great interest to model only a portion of the fluid domain to focus on the area of interest when using SPH to solve several fluid mechanics problems. This is why open boundaries are being researched.

The simplest way to deal with inlets/outlets is to use a buffer layer, where the values of the field at the open boundary are imposed on several layers of particle, so that the kernel of the free particles near the boundaries is complete [2]–[4]. However, this method can generate spurious shocks when particles are allowed to move freely after the buffer layer. It should be noted that Riemann solvers have already been used in this framework for Weakly Compressible SPH (WCSPH) [5], and it helped reduce the shocks. Nonetheless, modelling a complex boundary where the flow is not parrallel to the boundary remains difficult.

A slightly more flexible method has been developped by Kunz *et al.* [6], where mirror particles were used at the open boundaries. Through this method, Dirichlet pressure boundary conditions were succefully applied. Nonetheless, this work is just starting.

The most promising approach was developped by Kassiotis *et al.* [1], where the Semi-Analytical boundary conditions developped by Ferrand *et al.* [7] were extended to open boundaries. However, using this method both velocities and pressures were imposed, which tended to over-constrain the problem. This also limited the method to application where both fields are know at the open boundaries.

The work presented here will therefore use Riemann invariants to calculate compatible fields along the open boundaries. This will be validated using several test cases solving confined and free-surface problems.

## II. Reminders of the semi-analytical boundary conditions for weakly compressible SPH

### A. Notations

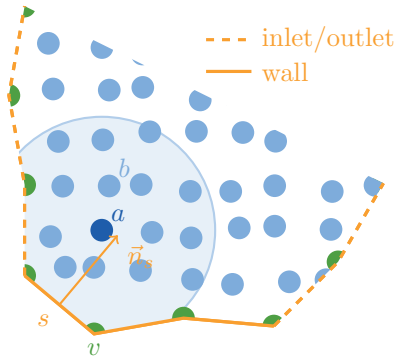


Fig. 1. Space discretization. Vertex particles are shown in green and segments in orange.

In terms of notations, the weakly compressible fluid domain $\Omega$ is discretised by a set of SPH fluid particles $\mathcal{F}$. These particles will be denoted by the subscript $(.)_a$ and it will be surrounded by neighbours $(.)_b$. The boundary $\partial\Omega$ is meshed. On the nodes of the mesh "vertex" particles $\mathcal{V}$ are placed. Along the elements of the mesh that connect the nodes, "segment particles" $\mathcal{S}$ are placed. The vertex particles will be denoted by $(.)_v$ and segment particles by $(.)_s$, see Fig. 1.

Each particle stores information such as mass $m_a$, position center $\boldsymbol{r}_a$, Lagrangian velocity $\boldsymbol{v}_a$ (*i.e.* the Lagrangian derivative of the position), Eulerian fluid velocity $\boldsymbol{u}_a$, density $\rho_a$, dynamic viscosity $\mu_a \equiv \nu\rho_a$, pressure $p_a$ and volume $V_a = m_a/\rho_a$.

It is important to underline that two sets of velocities are needed here, since the vertex particles and boundary segments at open boundaries are (most of the time) fixed in space but carry an information on the fluid velocity, namely $\boldsymbol{u}_v$ and $\boldsymbol{u}_s$. In other words, we have $\boldsymbol{u}_a = \boldsymbol{v}_a$ except for vertex particles and segments located onto the open boundaries. On

the other hand, this equality holds for wall segments and vertex particles, thanks to the no-slip condition. Furthermore, in our model all particle masses $m_a$ are constant in time, with the exception of the vertex particles of open boundaries, as detailed later.

Let $\rho_0$ be the reference density of the considered fluid. In the Weakly Compressible SPH approach used herein, the pressure field is deduced from the density field using Tait's equation of state [8], given as:

$$p_a = \frac{\rho_0 c_0^2}{\xi}\left[\left(\frac{\rho_a}{\rho_0}\right)^{\xi} - 1\right], \tag{1}$$

where $c_0$ is the numerical speed of sound and $\xi$ is taken to 7 for water.

The SPH interpolation used id the Wendland Kernel of order 5 [9]. The subscripts $(.)_{ab}$ generally denotes the difference of a quantity between the particles $a$ and $b$ (unless stated otherwise). For instance $\boldsymbol{u}_{ab} \equiv \boldsymbol{u}_a - \boldsymbol{u}_b$ and $\boldsymbol{r}_{ab} \equiv \boldsymbol{r}_a - \boldsymbol{r}_b$. Some exceptions are made, including the following notations: $w_{ab} \equiv w(\boldsymbol{r}_{ab})$ and $\boldsymbol{\nabla} w_{ab} \equiv \boldsymbol{\nabla}_a w(\boldsymbol{r}_{ab})$. The symbol $\boldsymbol{\nabla}_a$ denotes the gradient with respect to the position $\boldsymbol{r}_a$.

In addition, following the work of several authors [7], [10], an additional field denoted by $\gamma_a$ is used to take boundary terms into account. This field measures the part of the kernel support which is inside the computational domain and is defined as:

$$\gamma_a \equiv \int_{\Omega_a \cap \Omega} w(\boldsymbol{r}_a - \boldsymbol{r})\,\mathrm{d}\boldsymbol{r}. \tag{2}$$

The field $\gamma_a$ is computed from a dynamic governing equation [7]. The discrete SPH operators presented in the next section also require the computation of $\boldsymbol{\nabla}\gamma_a$, which is performed by a decomposition onto the boundary segments. Each segment contribution $\boldsymbol{\nabla}\gamma_{as}$ is defined as:

$$\boldsymbol{\nabla}\gamma_{as} \equiv \left(\int_s w(r)\,\mathrm{d}S\right)\boldsymbol{n}_s, \tag{3}$$

where $\boldsymbol{n}_s$ is the inward unit normal to the boundary segment $s$. Now $\boldsymbol{\nabla}\gamma_a$ is written as:

$$\boldsymbol{\nabla}\gamma_a = \sum_{s\,\in\,\mathcal{S}} \boldsymbol{\nabla}\gamma_{as}. \tag{4}$$

This gradient can be calculated analytically, see [7].

### B. Semi-Analytical boundary conditions

The Semi-Analytical boundary conditions were developped by Ferrand *et al.* [7] as a way to properly impose Neumann and Dirichlet boundary conditions. The vertices and segments are used to impose the desired boundary conditions after Gauss's theorem is applied to rewrite the SPH integrals of gradient and divergence operations, i.e.:

$$\frac{1}{\gamma_a}\int_\Omega \nabla(A_a) w_{ab} dV = \frac{1}{\gamma_a}\int_\Omega A_a \nabla w_{ab} dV - \int_{\partial\Omega} \nabla(A_a)\cdot n dS \tag{5}$$

This therefore leads space discretized differential operators. $\mathrm{G}_a^{\gamma,+}\{A_b\}$ which is a boundary corrected gradient of the discrete scalar field $\{A_b\}$, $D_a^{\gamma,-}\{\boldsymbol{A}_b\}$ which is a boundary corrected divergence of the discrete vector field $\{\boldsymbol{A}_b\}$, and $L_a^{\gamma}\{B_b, A_b\}$ which is a boundary corrected Laplacian of the discrete scalar (or vector) field $\{A_b\}$ with discrete diffusion field $\{B_b\}$. They are defined by the following equations [7]:

$$\mathrm{G}_a^{\gamma,+}\{A_b\} \equiv \frac{\rho_a}{\gamma_a}\sum_{b\,\in\,\mathcal{P}} m_b\left(\frac{A_a}{\rho_a^2} + \frac{A_b}{\rho_b^2}\right)\boldsymbol{\nabla} w_{ab} - \frac{\rho_a}{\gamma_a}\sum_{s\,\in\,\mathcal{S}}\left(\frac{A_a}{\rho_a^2} + \frac{A_s}{\rho_s^2}\right)\rho_s \boldsymbol{\nabla}\gamma_{as}, \tag{6}$$

$$\mathrm{D}_a^{\gamma,-}\{\boldsymbol{u}_b\} \equiv -\frac{1}{\gamma_a\rho_a}\sum_{b\in\mathcal{P}} m_b \boldsymbol{u}_{ab}\cdot\boldsymbol{\nabla} w_{ab} + \frac{1}{\gamma_a}\sum_{s\in\mathcal{S}} \boldsymbol{u}_{as}\cdot\boldsymbol{\nabla}\gamma_{as}, \tag{7}$$

$$\mathrm{L}_a^{\gamma}\{B_b, A_b\} \equiv \frac{1}{\gamma_a}\sum_{b\,\in\,\mathcal{P}} V_b 2\overline{B}_{ab}\frac{A_{ab}}{r_{ab}^2}\mathbf{r}_{ab}\cdot\boldsymbol{\nabla} w_{ab} - \frac{1}{\gamma_a}\sum_{s\,\in\,\mathcal{S}}\left(B_s\boldsymbol{\nabla}A_s + B_a\boldsymbol{\nabla}A_a\right)\cdot\boldsymbol{\nabla}\gamma_{as}. \tag{8}$$

The factor $\overline{B}_{ab}$ is build with $B_a$ and $B_b$. In most of the SPH literature, it is taken as their arithmetic mean. However, to ensure continuity of shear flux, *i.e.* $B_a\boldsymbol{\nabla}A_a\cdot\boldsymbol{r}_{ab} = B_b\boldsymbol{\nabla}A_b\cdot\boldsymbol{r}_{ab}$, it is taken here as their harmonic mean:

$$\overline{B}_{ab} = \frac{2B_aB_b}{B_a + B_b}. \tag{9}$$

### C. Volume diffusion correction

Furthermore, it should be noted that a volumic diffusion term is applied, as the pressure and velocities are collocated, *i.e.* stored at the same points (the particle positions), and therefore require stabilization. In the present work the stabilization factor is derived from the pressure-velocity coupling available in the literature for Finite Elements mesh-based method, namely Brezzi and Pitkäranta [11], which was adapted to Semi-Analytical SPH boundaries by Ghaitanellis *et al.* [12]. This volumic diffusion is weighed by a factor $\Lambda$.

### D. Treating open boundaries

The work by Kassiotis *et al.* [1] extended these boundary conditions to deal with open boundaries. The first step was to properly solve the continuity equation. The continuity equation will be solved as a summation of the densities, as presented by Villa [13], but where particular care is given to ensure that the time integration of Eulerian fields takes into account

the Lagrangian fields. This gives the following equation for continuity:

$$\rho_a^{n+1} = \frac{1}{\gamma_a^{n+1}} \left( \gamma_a^n \rho_a^n + d_a^{\text{i/o}} \right). \tag{10}$$

Where $d_a^{\text{i/o}}$ represents the added terms in the continuity equation, i.e.:

$$\begin{aligned} d_a^{\text{i/o}} = & \sum_{b \in \mathcal{P}^n} m_b^n \left( w_{ab}^{n+1} - w_{ab}^n \right) \\ & + \frac{\rho_a^n}{2} \sum_{s \in \mathcal{S}^{\text{i/o}}} \left[ \boldsymbol{\nabla} \gamma_{as} \left( \boldsymbol{r}_{as}^n + \delta \boldsymbol{r}_s^{\text{i/o}} \right) + \boldsymbol{\nabla} \gamma_{as} \left( \boldsymbol{r}_{as}^n \right) \right] \cdot \delta \boldsymbol{r}_s^{\text{i/o}} \\ & + \sum_{v \in \mathcal{V}^{\text{i/o}}} m_v^n \left[ w_{av}^n - w \left( \boldsymbol{r}_{av}^n + \delta \boldsymbol{r}_v^{\text{i/o}} \right) \right] \end{aligned} \tag{11}$$

Where the virtual displacements, $\delta \boldsymbol{r}_v^{\text{i/o}}$ and $\delta \boldsymbol{r}_s^{\text{i/o}}$ are defined by:

$$\delta \boldsymbol{r}_v^{\text{i/o}} = \Delta t \left( \boldsymbol{u}_v^n - \boldsymbol{v}_v^n \right) \tag{12}$$

$$\delta \boldsymbol{r}_s^{\text{i/o}} = \Delta t (\boldsymbol{u}_s^n - \boldsymbol{v}_s^n) \tag{13}$$

To allow inflows and outflows, the masses of the vertices is allowed to vary. The mass variations are calculated using the following equation:

$$m_v^{n+1} = m_v^n + \Delta t \dot{m}_v^n + \delta m_v^n, \qquad \forall v \in \mathcal{V}^{\text{i/o}}, \tag{14}$$

Where the mass flux $\dot{m}_v^n$ is calculated using the following equation:

$$\dot{m}_v = \frac{1}{2} \sum_{s \in \mathcal{N}_{sv}^{i/o}} \rho_s S_s (\boldsymbol{u}_s - \boldsymbol{v}_s) \cdot \boldsymbol{n}_s, \qquad \forall v \in \mathcal{V}^{\text{i/o}}, \tag{15}$$

The symbol $\delta m_v^n$ represents the mass variations that corresponds to particle creation/deletion. Particles are created whenever the masses of a vertex particle exceeds a threshold, and they are deleted whenever fluid particles cross an open boundary. More details are given in Kassiotis *et al.* [1].

## III. Imposing compatible pressure and velocity fields along the open boundaries

In the previous sections, the basis to properly allow particles to enter and leave a domain has been defined. However, when dealing with open boundaries compatible boundary conditions need to be imposed. To do so, a linearised Riemann problem will be solved.

This methodology is widely used in the literature for Finite Volumes, and the approach chosen here follows the work of Blondel *et al.* [14], here with simplifying assumptions of barotropic fluid and subsonic flow. The latter assumption is justified by the fact that weakly compressible SPH assumes the speed of sound to be significantly larger than the flow velocity.

Let us consider a segment $s$ on an open boundary and work in the local reference frame of space dimension $d$ relative to $s$, denoted by $(\boldsymbol{n}, \boldsymbol{t}_1, \cdots, \boldsymbol{t}_{d-1})$, $\boldsymbol{n}$ being the local normal unit vector and $\boldsymbol{t}_k$ the tangential unit vectors. In this section, for simplicity we will drop the label $s$ relative to all fields. Let us start from the Euler equations, and neglect variations along the tangents of $s$, to write the linearised Riemann problem (LRP):

$$\frac{\partial \boldsymbol{Y}}{\partial t} + \mathbf{B}(\boldsymbol{Y}) \frac{\partial \boldsymbol{Y}}{\partial n} = \mathbf{0}, \tag{16}$$

where the unknown vector is defined as:

$$\boldsymbol{Y} \equiv \begin{pmatrix} \rho \\ u_n \\ u_{t_1} \\ \vdots \\ u_{t_{d-1}} \end{pmatrix} = \begin{pmatrix} \rho \\ \boldsymbol{u} \cdot \boldsymbol{n} \\ \boldsymbol{u} \cdot \boldsymbol{t}_1 \\ \vdots \\ \boldsymbol{u} \cdot \boldsymbol{t}_{d-1} \end{pmatrix}, \tag{17}$$

and the matrix $\mathbf{B}$ as:

$$\mathbf{B}(\boldsymbol{Y}) \equiv \begin{pmatrix} u_n & \rho & 0 & \cdots & 0 \\ \frac{c^2}{\rho} & u_n & 0 & \cdots & 0 \\ 0 & 0 & u_n & 0 & \cdots \\ \vdots & \vdots & 0 & \ddots & 0 \\ 0 & 0 & \cdots & 0 & u_n \end{pmatrix}. \tag{18}$$

Furthermore the speed of sound $c$ is defined from the state Equation (1) as:

$$c \equiv \sqrt{\frac{\partial p}{\partial \rho}} = c_0 \left( \frac{\rho}{\rho_0} \right)^{\frac{\xi - 1}{2}}. \tag{19}$$

The eigenvalues of $\mathbf{B}$ are $\lambda_{-1} \equiv u_n - c$, $\lambda_0 \equiv u_n$ (with a multiplicity $d-1$) and $\lambda_{+1} \equiv u_n + c$.

The Eigenvalues and Eigenvectors will be used to calculate compatible fields. Along an open boundary there is a discontinuity between the exterior state (upon which we want to impose our values) and the interior state (*i.e.* the fluid domain). The eigenvalues of the problem, $\lambda_i$, represent the slope of the characteristic curves of the Riemann problem (see Fig. 2). These curves represent discontinuities between the states on their right and left sides (for example the wave $\lambda_0$ is a discontinuity between the data state $\mathbf{Y}_1$ and $\mathbf{Y}_2$). The Generalized Riemann Invariants (GRI) define quantities that are conserved across certain characteristic curves (we will see which ones afterwards), and therefore can help link the exterior and interior state. The GRIs are calculated from the relations defined by Jeffrey [15]:

$$R_\lambda \equiv \frac{dY_1}{V_{r,1}^\lambda} = \frac{dY_2}{V_{r,2}^\lambda} = ... = \frac{dY_d}{V_{r,d}^\lambda}, \tag{20}$$

where $Y_i$ is a components of vector $\mathbf{Y}$, $V_{r,i}^\lambda$ is a components of the right eigenvector of $\mathbf{B}$ associated to the eigenvalue $\lambda$ and $R_\lambda$ is its corresponding GRI.

The GRI corresponding to the celerities $\lambda_{-1}$, $\lambda_0$ and $\lambda_{+1}$ are respectively denoted by $R_{-1}$, $R_0$ and $R_{+1}$:

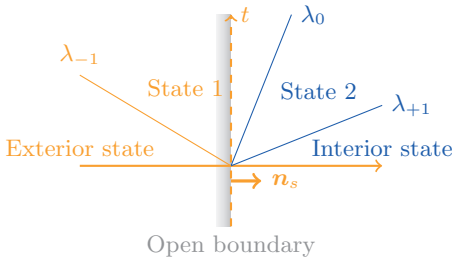


(a) Inlet

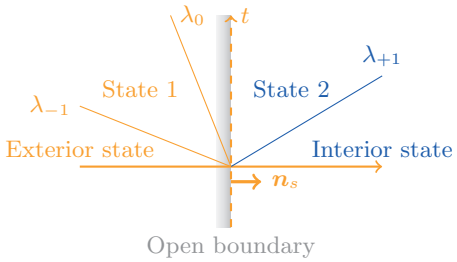


(b) Outlet

Fig. 2. Sketches of the Riemann problems.

$$R_{-1} \equiv u_n + \psi, \tag{21}$$
$$R_0 \equiv u_n, \tag{22}$$
$$R_{+1} \equiv u_n - \psi, \tag{23}$$

where:

$$\psi \equiv \int_{\rho_0}^{\rho} \frac{c}{\tilde{\rho}} \mathrm{d}\tilde{\rho}, \tag{24}$$

*i.e.*:

$$\psi = \begin{cases} \dfrac{2c_0}{\xi - 1}\left(\dfrac{\rho}{\rho_0}\right)^{\frac{\xi-1}{2}} & \text{if } \xi > 1 \\ c_0 \ln \dfrac{\rho}{\rho_0} & \text{if } \xi = 1: \end{cases} \tag{25}$$

Going back to the problem at hand, the state of the segment value $\boldsymbol{Y}_s$ is either defined by the first state (see Fig. 2a) or by the second state (see Fig. 2b) which respectively correspond to $\lambda_0 = u_n \geq 0$ (ingoing mass flux) and $\lambda_0 = u_n < 0$ (outgoing mass flux). One should bear in mind that $\lambda_{-1}$ will always be negative and $\lambda_{+1}$ always positive as the flow is assumed to be subsonic.

Wave $\lambda_0$ is known as a contact discontinuity, *i.e.* $\lambda_0$ in state 1 is equal to $\lambda_0$ in state 2 ($\lambda_{0,1} = \lambda_{0,2}$) [16]. This implies that $u_{n,1} = u_{n,2}$, which is consistent with the GRI relations defined in equation (20). Through these relations it is also considered that $d\rho = 0$ across $\lambda_0$. Therefore $\rho_1 = \rho_2$, but also $p_1 = p_2$ as the pressure is defined by Equation (1).

Therefore to link the fluid velocity along the normal of the segment and the pressure, one needs only to find a relation between state 2 and the interior state; *i.e.* across the characteristc wave $\lambda_{+1}$ (the tangential velocities will be dealt with later on). As defined by Toro [16] the characteristic wave $\lambda_{+1}$ can belong to three possible type of discontinuity:

1) **Contact wave**
In this case the characteristics are parallel in both states, this means that the following condition is true:
$$\lambda_{+1,2} = \lambda_{+1,int}, \tag{26}$$
and the GRI relations hold across the characteristic wave:
$$R_{+1,2} = R_{+1,int}. \tag{27}$$

2) **Expansion (or rarefaction) wave**
In this case the characteristics are diverging, and the two data states are connected through a *smooth transition*. This case is defined by the following condition:
$$\lambda_{+1,2} < \lambda_{+1,int}, \tag{28}$$
and the GRI relations hold across the characteristic wave:
$$R_{+1,2} = R_{+1,int}. \tag{29}$$

3) **Shock wave**
In this case the characteristics are converging towards the wave $\lambda_{+1}$, meaning that this case is defined by the following condition:
$$\lambda_{+1,2} > \lambda_{+1,int}. \tag{30}$$
In this case the GRI relations do not hold across the characteristic wave, and therefore the Rankine-Hugoniot relationships have to be used:
Conservation of mass:
$$\rho_2 u_{n,2} = \rho_{int} u_{n,int}, \tag{31}$$
Conservation of momentum:
$$p_2 + \rho_2 u_{n,2}^2 = p_{int} + \rho_{int} u_{n,int}^2. \tag{32}$$

For the case of the tangential velocities the Riemann invariants relations make it possible to write $du_{t_1} = ... = du_{t_{d-1}} = 0$ across the wave $\lambda_{+1}$ (we will assume these relations still hold in the case of a shock). Therefore the tangential velocities are equal between state 2 and the interior state. However, the wave $\lambda_0$ acts as a discontinuity.

Therefore if the problem is that of an inlet then the discontinuity prevents a relationship between state 2 and state 1 to be defined for these velocities, all that is known is that $du_{t_1} = ... = du_{t_{d-1}} = Const$. This means that these velocities need to be defined by the user for inlet open boundaries. However for the case of an outlet then the $\lambda_0$ will be assumed to be a "ghost" wave and the exterior tangential velocities will be assumed to be equal to the tangential velocities of state 1 and 2, and therefore equal to the velocities of the interior state.

In mesh-based methods, such as Finite Volumes, knowing the interior state data is simple as boundary segments are only connected to one element. However in the SPH formulation

there is more than one fluid particle connected to a boundary segment. Therefore defining the interior state is non-trivial. The method chosen is to use the SPH interpolations as defined by Ferrand *et al.* [7]:

$$p_{s,int} = \frac{1}{\alpha_s} \sum_{b \in \mathcal{F}} V_b p_b w_{bs}, \tag{33}$$

where, as a reminder, $\mathcal{F}$ contains only fluid particles and $\alpha_s$ is the Shepard filter defined for a segment $s$ by:

$$\alpha_s = \sum_{b \in \mathcal{F}} V_b w_{bs}. \tag{34}$$

Similarly, the interior velocity is defined as:

$$\boldsymbol{u}_{s,int} = \frac{1}{\alpha_s} \sum_{b \in \mathcal{F}} V_b \boldsymbol{u}_b w_{bs}. \tag{35}$$

Finally, the density will be calculated using Equation (1).

Therefore, along open boundaries, once one of the fields (velocity or pressure) has been imposed it is possible to estimate the type of discontinuity of the characteristic wave $\lambda_{+1}$, and calculate the corresponding field (pressure or velocity respectively) using either the GRI or Rankine-Hugoniot relationships.

## IV. Validation cases

### A. Rapidly expanding pipe

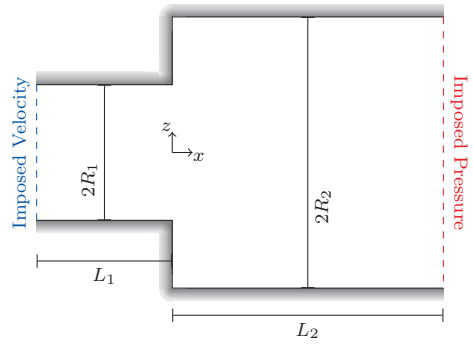


Fig. 3. Configuration of the rapidly expanding pipe. The origin is placed at the beginning of the second pipe, and on the central axis of the pipes.

For the first validation case, the flow from a small pipe (named pipe 1) will enter a large pipe (named pipe 2), creating a sudden expansion of the flow. See Fig. 3 for details on the geometry. Far from the expansion, the flow should follow the Hagen-Poiseuille equations, which for a flow between two infinite plates is given by:

$$u_x = U_{max}\left(1 - \frac{z^2}{R^2}\right), \tag{36}$$

$$\frac{dP}{dx} = -\frac{2\rho_0 \nu U_{max}}{R^2}. \tag{37}$$

Where the origin of $z$ is on the center pipe axis, $R$ is the radius of the pipe and $U_{max}$ is the maximum velocity. To ensure that the flow stays laminar, this maximum velocity will be defined according to a Reynolds number Re:

$$U_{max} = \frac{\nu \mathrm{Re}}{2R}. \tag{38}$$

A Poiseuille flow velocity profile will therefore be imposed on the inlet, and a constant pressure will be imposed on the outlet. The geometrical parameters are chosen to correspond to one of the experiments presented by Hammad *et al.* [17]: $R_1 = 0.13$ m, $L_1 = 3R_1$, $R_2 = 2R_1$ and $L_2 = 4R_2$. The particle spacing $\Delta r = R_1/26$ and the physical parameters chosen are $\rho_0 = 1190$ kg.m$^{-3}$, $\nu = 3.19 \times 10^{-5}$ m$^2$.s$^{-1}$ and Re $= 20.6$. The numerical parameters are $c_0 = 0.03$ m.s$^{-1}$ and $\Lambda = 0.1$. A background pressure is used to help the flow stabilize.

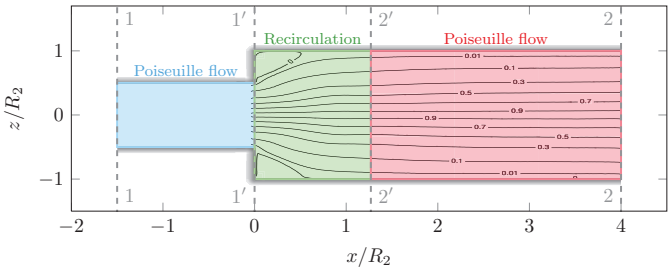


Fig. 4. The three regions in the rapidly expanding pipe that can be defined to claculate the head loss from the simulated flow.

Looking at the streamlines of the flow, it can be separated into 3 regions: a Poiseuille flow inside pipe 1, a recirculation zone created by the sudden expansion and a Poiseuille flow inside pipe 2 (see Fig. 4). One can estimate the head loss in each section using the same method as Hérard and Martin [18], i.e the expected head loss is therefore equal to the sum of head loss of the Poiseuille flows, and Borda-Carnot head loss in the recirculation zone.

Defining the head of the flow by:

$$H = \frac{\widehat{U}^2}{2g} + \frac{P}{g\rho_2}. \tag{39}$$

Where $\widehat{U}^2 = 1/(2R)\int_{-R}^{R} U^2 d\tilde{z}$, $P = 1/(2R)\int_{-R}^{R} p d\tilde{z}$. The theoretical head loss between the inlet and the outlet is thus equal to:

$$H_1 - H_2 = \frac{1}{2g}\left(\widehat{U}_1 - \widehat{U}_2\right)^2 + \frac{1}{g\rho_2}\left(P_1 - P_{1'}\right) + \frac{1}{g\rho_2}\left(P_2 - P_{2'}\right) \tag{40}$$

Where the subscript represent the interface between different zones of the flow, see Fig. 4.

Fig. 5 shows the head along the $x$-axis. Extracting the simulated head loss and calculating the theoretical head loss gives:

- Head loss from simulations = $5.04 \times 10^{-7}$ m
- Theoretical head loss = $5.00 \times 10^{-7}$ m

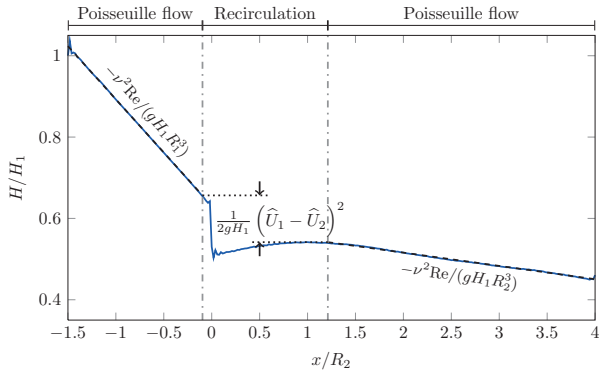


Fig. 5. Head profile plotted along the $x$-axis of the rapidly expanding pipe. The blue line is the computed head, the dashed lines show the theoretical head gradient of the Poisseuille flows (from Equations 37 and 38) and the arrows around the dotted line shows the head loss from the Borda-Carnot equation.

Therefore, the simulated head loss has less than a 1% difference with the theoretical head loss.

### *B. 2-D periodic free-surface water wave*

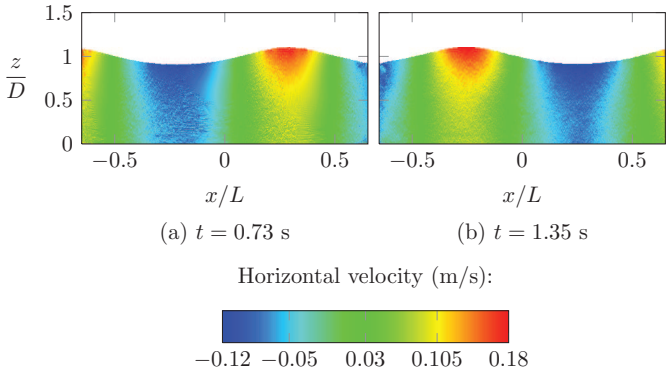


Fig. 6. Propagation of a regular waves on a flat bottom with open boundaries given at 2 instances. A time varying velocity profile is prescribed on both vertical boundaries so they alternate between inlets and outlets.

The next test case shows that these new open boundary conditions can be used for both inflows and outflows, and that open boundaries can alternate between the two without any difficulties, even with a free surface. To do so periodic water waves propagating on a flat bed will be imposed. The waves imposed are calculated from the $5^{\text{th}}$ order solution to Stokes wave theory given by Fenton [19].

The following symbols will be used: $\eta$ is the free surface elevation (with the water depth $h = D + \eta$), $A$ is the wave amplitude (i.e. half of the wave height), $D$ is the mean water depth, $g$ is the acceleration due to gravity, $k$ is the wave number (defined as $k = 2\pi/L$, where $L$ is the wave length), $c$ is the wave velocity. The wave period $T$ can be calculated from the wave number and wave velocity, i.e. $T = 2\pi/(kc)$. Furthermore the $z$-axis has its origin at the bed.

For the present test case a depth of 0.5 m, an amplitude of 0.05 m and a wave length of 2.5 m have been chosen. Furthermore there will be no mean current in the flow. The Ursell number for this case is $2AL^2/d^3 = 5 \ll 32\pi^2/3$, which would mean that linear wave theory is applicable. However, a higher order solution is used, as phase difference can occur after several time period. Finally, in the simulation the fluid viscosity $\nu$ is set to $10^{-6}$ $\mathrm{m^2 s^{-1}}$, the particle spacing $\Delta r$ is set to one tenth of the amplitude and the numerical parameters are $c_0 = 20$ $\mathrm{m.s^{-1}}$ and $\Lambda = 0.1$. An illustration of this test case can be found in Fig. 6 where it is shown that the open boundaries alternate between inlets and outlets.

A simulation with periodic boundary conditions will be first be run (*i.e.* when particles exit the boundary on one side they enter on the other). These results will then compared to a simulation where the fluid velocities calculated from the analytical solution [19] will be imposed along the normal of the open boundaries, and Riemann invariants will be used to calculate the pressure. It should be noted that if both the pressure and the velocities would be imposed, then the problem would be overconstrained and particles would exit the domain.

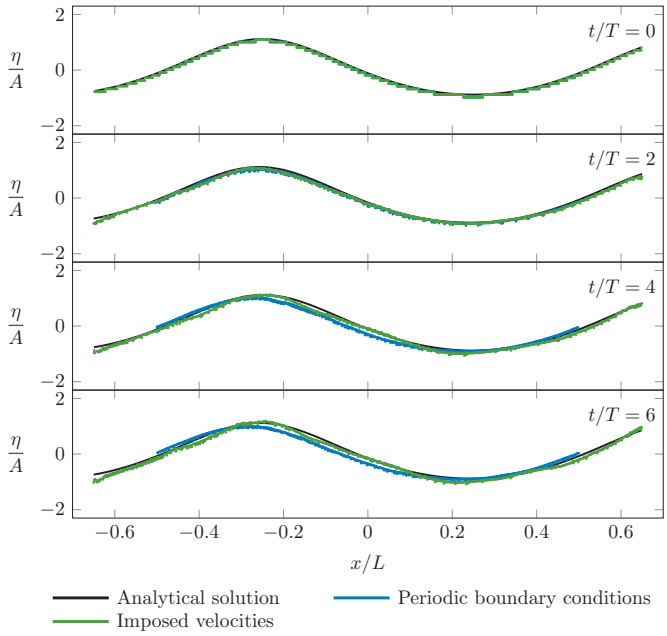


Fig. 7. Free surface particles for simulations using different boundary conditions compared to the analytical solution by Fenton [19].

Plots of the free surface are then presented in Fig. 7. The first conclusion is that even after several wave periods the free surface stays very close to the analytical solution for all type of boundaries. With periodic boundary conditions, the wave seems to be slightly slower than the analytical solution and it forces the domain to be a multiple of the wave length. This is not the case with the open boundary conditions (as can be seen from the fact that the green free surface particles extend over a longer range than the blue free surface particles).

Furthermore, let us define the error on the free surface using the following equation:

$$\varepsilon_\eta = \sqrt{\frac{1}{N_{\mathcal{FS}}} \sum_{a \in \mathcal{FS}} \frac{(\eta_{sim} - \eta)^2}{A^2}}, \tag{41}$$

where $\mathcal{FS}$ represents the free surface particles, $N_{\mathcal{FS}}$ is the number of free surface particles, $\eta_{sim}$ is the free surface elevation of the simulations and $\eta$ is the analytical solution by Fenton [19].

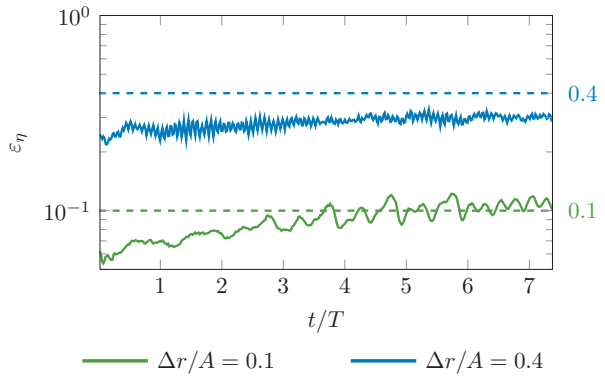


Fig. 8. Errors on the free surface for simulations with an imposed velocity profile on the open boundaries for two particle spacing $\Delta r$. The dashed line show the two values $\Delta r/A$.

These errors are plotted over time in figure 8, which shows that for these discretisation the error (the solid line) is of the order of the particle spacing (the dashed line). Unfortunatly, this is not the case for smaller particle size as an unstability develops, increasing the error. These instabilities appear as a checkerboarding effect close to the inlets, and work on the volumic diffusion term close to open boundaries will be neccesary in the future to reduce those errors for very refined simulations.

### C. 3D solitary wave

The Riemann invariants become particularly useful when the boundary conditions are not well known, or not easy to predict. To illustrate this concept, a test case for the propagation of a solitary wave on a bed with a step, that will cause it to break will be presented.

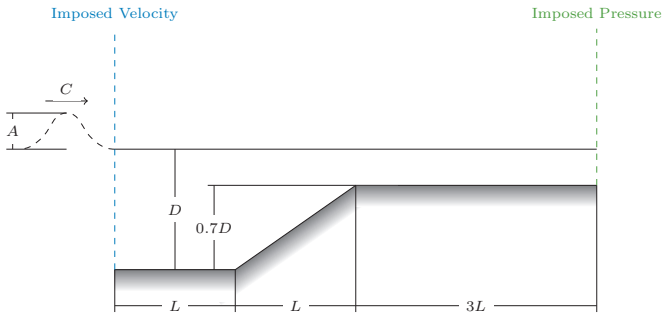


Fig. 9. Side view of the 3D solitary wave on a sloped domain configuration.

At the inlet a wave front calculated from the 2D Korteveg-De Vries solitary wave equation [20] will enter the domain at an angle $\theta$:

$$\eta(x,y,t) = A\,\mathrm{sech}^2\Big(k\,[x\cos\theta + y\sin\theta - ct - x_0]\Big), \tag{42}$$

$$h(x,y,t) = D + \eta(t), \tag{43}$$

$$p(x,y,z,t) = \rho g(z - h(t)), \tag{44}$$

$$u_x(x,y,z,t) = c\frac{\eta(t)}{h(t)}\cos(\theta), \tag{45}$$

$$u_y(x,y,z,t) = c\frac{\eta(t)}{h(t)}\sin(\theta), \tag{46}$$

$$u_z(x,y,z,t) = \frac{z}{h(t)}\frac{\partial \eta}{\partial t}(t). \tag{47}$$

where $A$ is the amplitude and $x_0$ is wave shifting length. The wave number and celerity are computed as $k = \sqrt{3A/4D^3}$, $c = \sqrt{g(A+D)}$.

At the outlet a hydrostatic pressure corresponding to the reference level $D$ will be imposed and the velocities will be calculated using Riemann invariants.

The geometry chosen for the test case illustrated in Fig. 9 is a the reference depth $D = 0.6m$, wave amplitude $A = D/2$ and characteristic length $L = 2.5D$. The wave shifting length is set to ensure that the waves are not in the domain at the initialisation, i.e. $x_0 = -4k$.

The fluid viscosity $\nu$ is set to $10^{-6}$ m$^2$s$^{-1}$, the particle spacing will be set to one thirtieth of the amplitude ($\Delta r = A/30$) and the numerical parameters are $c_0 = 20$ m.s$^{-1}$ and $\Lambda = 0.1$.

The evolution of the solitary wave within the domain at different instances is shown in figure 10. It shows that the step causes the wave to break, creating a highly disturbed flow to exit the domain. Nonetheless, through the use of Riemann invariants (and imposing a hydrostatic pressure) the wave exits the domain without any reflections showing the high flexibility of these new open boundary conditions.

## V. Conclusion

In a previous article, Kassiotis *et al.* [1], the Unified Semi-Analytical boundary conditions have been extended to treat complex inlets and outlets without spurious shocks. The work presented here has improved on the method by allowing compatible pressure and velocity fields to be imposed on the open boundaries. This was done through the use of Riemann invariants.

This work has been validated on three test cases; a rapidely expanding pipe flow, periodic waves and a breaking solitary wave. The first test case showed that the fields calculated using the Riemann invariants were indeed compatible. The second test case showed that unsteady boundary conditions were effectively imposed. Finally, the last test case showed that these open boundary conditions can be used to allow complex flows to exit the domain.

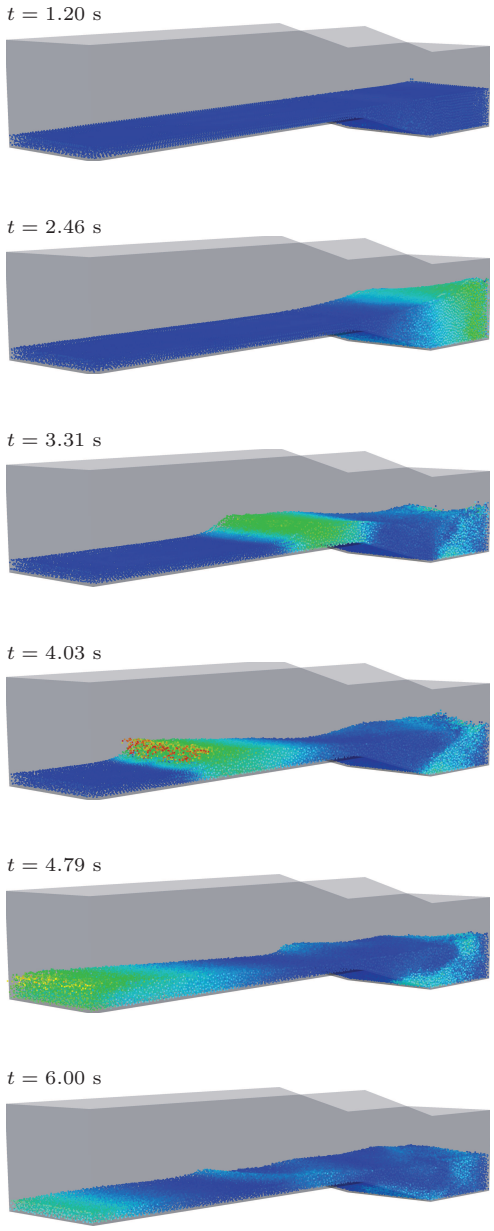


Fig. 10. Propagation of a solitary wave on a bed with a step. The fields plotted represent the velocity magnitude. The velocities range from 0 to 3 m/s.

In all cases this formulation of open boundaries in a Smoothed Particle Hydrodynamics framework have proved to be very adaptative to complex confined and free-surface flows. Furthermore, since these boundary conditions produce smooth fields near the open boundaries, these boundary conditions will be particularly suited for coupling, as small perturbations near the shared boundary can lead to instabilities [21].

## ACKNOWLEDGMENT

The authors would like to thank Dr. Ben Rogers for his inputs while the method was developped.

## REFERENCES

[1] C. Kassiotis, D. Violeau, and M. Ferrand, "Semi-analytical conditions for open boundaries in smoothed particle hydrodynamics," in *8th International SPHERIC Workshop*, Trondheim, 2013, pp. 28–35.
[2] R. Vacondio, B. D. Rogers, P. K. Stansby, and P. Mignosa, "SPH modeling of shallow flow with open boundaries for practical flood simulation," *Journal of Hydraulic Engineering*, vol. 138, no. 6, pp. 530–541, 2011.
[3] B. Bouscasse, S. Marrone, A. Colagrossi, and A. Di Mascio, "Multi-purpose interfaces for coupling sph with other solvers," in *8th SPHERIC International Workshop*, 2013.
[4] S. Braun, L. Wieth, R. Koch, and H.-J. Bauer, "A framework for permeable boundary conditions in sph: Inlet, outlet, periodicity," in *10th SPHERIC International Workshop*, 2015.
[5] O. Mahmood, C. Kassiotis, D. Violeau, B. D. Rogers, and M. Ferrand, "Absorbing inlet/outlet boundary conditions for SPH 2-D turbulent free-surface flows," in *7th SPHERIC International Workshop*, 2012.
[6] P. Kunz, M. Hirschler, M. Huber, and U. Nieken, "Inflow / outflow with Dirichlet boundary conditions for pressure in ISPH," *Journal of Computational Physics*, Submitted.
[7] M. Ferrand, D. R. Laurence, B. D. Rogers, D. Violeau, and C. Kassiotis, "Unified semi-analytical wall boundary conditions for inviscid, laminar or turbulent flows in the meshless SPH method," *International Journal for Numerical Methods in Fluids*, vol. 71, no. 4, pp. 446–472, 2012.
[8] P. G. Tait, "Report on some of the physical properties of fresh water and sea water," *Report on the Voyage of Challenger, Physics and Chemistry*, vol. 2, pp. 1–76, 1888.
[9] H. Wendland, "Piecewise polynomial, positive definite and compactly supported radial functions of minimal degree," *Advances in Computational Mathematics*, vol. 4, pp. 1414–1421, 1995.
[10] S. Kulasegaram, J. Bonet, R. W. Lewis, and M. Profit, "A variational formulation based contact algorithm for rigid boundaries in two-dimensional SPH applications," *Computational Mechanics*, vol. 33, p. 316325, 2004.
[11] F. Brezzi and J. Pitkäranta, "On the stabilization of finite element approximations of the stokes equations," in *Efficient Solutions of Elliptic Systems*, ser. Notes on Numerical Fluid Mechanics, W. Hackbusch, Ed. Vieweg+Teubner Verlag, 1984, vol. 10, pp. 11–19.
[12] A. Ghaitanellis, D. Violeau, M. Ferrand, A. Leroy, and A. Joly, "Application of the unified semi-analytical wall boundary conditions to multi-phase sph," in *10th SPHERIC International Workshop*, 2015.
[13] J. P. Vila, "On particle weighted methods and smooth particle hydrodynamics," *Mathematical Models and Methods in Applied Sciences*, vol. 9, no. 2, pp. 161–209, 1999.
[14] F. Blondel, B. Audebert, T. Pasutto, and M. Stanciu, "Condensation models and boundary conditions for non-equilibrium wet steam flows," *International Journal on Finite Volumes*, vol. 10, pp. 1–53, 2013.
[15] A. Jeffrey, *Quasilinear Hyperbolic Systems and Waves*. London: Pitman, 1976.
[16] E. F. Toro, *Riemann solvers and numerical methods for fluid dynamics*. London: Springer, 2009.
[17] K. J. Hammad, M. V. Ötügen, and E. B. Arik, "A PIV study of the laminar axisymmetric sudden expansion flow," *Experiments in Fluids*, vol. 26, pp. 266–272, 1999.
[18] J.-M. Hérard and X. Martin, "An integral approach to compute compressible fluid flows in domains containing obstacles," *International Journal on Finite Volumes*, pp. hal–01 166 478, Preprint.
[19] J. D. Fenton, "A fith-order Stokes theory for steady waves," *Journal of Waterway, Port, Coastal and Ocean Engineering*, vol. 111, no. 2, pp. 216–234, 1985.
[20] R. G. Dean and R. A. Dalrymple, *Water wave mechanics for engineers and scientists*, ser. Advanced Series on Ocean Engineering. Singapore: World Scientific, 1991, vol. 2.
[21] C. Kassiotis, M. Ferrand, D. Violeau, B. D. Rogers, P. K. Stansby, M. Benoit *et al.*, "Coupling SPH with a 1-D Boussinesq-type wave model," in *6th International SPHERIC Workshop*, 2011, pp. 241–247.